Tunable, Dual-Gate, Silicon-on-Insulator (SOI) Nanoelectromechanical Resonators

Lin Yu, Hossein Pajouhi, Molly R. Nelis, *Member, IEEE*, Jeffrey F. Rhoads, and Saeed Mohammadi, *Senior Member, IEEE*

***Abstract*—Resonant nanoelectromechanical systems (NEMS) have the potential to have significant impact in mass sensing, signal processing, and field detection applications, if the challenges associated with processing, material, and geometric variability can be mitigated. The research presented here details a breakthrough in the design and development of resonant NEMS aimed at addressing these challenges. Specifically, this study details the fabrication, characterization, and tuning of dual-gate silicon nanoelectromechanical resonators, which are transduced electrostatically and realized with close to 100% yield. These devices are fabricated on a silicon-on-insulator (SOI) substrate using only top-down microfabrication techniques and can be easily integrated with SOI-CMOS transistors, enabling the development of fully integrated CMOS-NEMS with highly tunable nonlinear frequency response characteristics.**

***Index Terms*—Dual-gate nanoresonators, electrostatic tuning, nonlinear tuning, silicon nanowire.**

I. Introduction

NANOELECTROMECHANICAL systems (NEMS) are eliciting great interest because they allow access to microwave frequencies and nanosecond response times, amongst other pertinent metrics [1]–[5]. These unprecedented properties are fueling the potentially ground-breaking application of NEMS in analog and RF signal processing [6]–[9], nanomechanical electrometry [10], and chemical and biological sensing [11]–[22]. To date, most NEMS resonators have been fabricated using bottom-up carbon nanotube or nanowire (NW) synthesis, followed by low-temperature top-down microfabrication [2]–[4], [22]–[28]. While this approach can be adopted for post-CMOS device fabrication, it is quite susceptible to processing, material, and geometric variability [29], which leads to irreproducible near-resonant response characteristics and, ultimately, prohibits predictive device design.

Resonant NEMS devices fabricated using only a top-down approach have also been reported [10], [30]–[34]. However, with perhaps one exception [34], these devices cannot be fabricated and integrated as a single-chip solution in mass sensing or signal processing applications, as technologies that are not based on Si resonators (including piezoelectric NEMS devices) are generally incompatible with CMOS processing, and devices which rely on magnetomotive or optical transduction typically require additional hardware to fully characterize their near-resonant response.

This study describes the design, development, and characterization of electrostatically transduced nanoelectromechanical resonators which are aimed at addressing the aforementioned constraints and are fabricated using only top-down microfabrication, as realized via a silicon-on-insulator (SOI) process flow. SOI-CMOS technology is widely employed in the development of low-power digital microprocessors, such as those used in mobile computing and communication platforms. The selective nature of silicon/silicon dioxide (Si/SiO_2) etching which enables the fabrication of these devices also allows for the development, implementation, and on-chip integration of SOI-NEMS. The dual-gate silicon devices detailed here are reproducible and reliable, have been fabricated with near 100% yield (excluding the outer perimeter of the chip), and can be easily integrated with SOI-CMOS transistors, enabling the development of fully integrated CMOS-NEMS with highly tunable in-plane and out-of-plane, nonlinear frequency response characteristics.

II. Device Fabrication

SOI wafers with a 110 nm device layer and 144 nm buried oxide layer are used in this study. The wafers are slightly doped with boron ($\rho = 14$–$20\ \Omega\cdot$cm). Prior to device fabrication, the SOI wafers are implanted with phosphorous. An impurity dose of $1 \times 10^{13}\ \text{cm}^{-2}$ and an implantation energy of 40 keV are employed to ensure that the peak concentration (with an estimated doping density of $10^{18}\ \text{cm}^{-3}$) appears in the middle of the device layer. After ion implantation, the wafers are annealed at 1050 °C in a nitrogen ambient for 60 s using a rapid thermal annealing (RTA) furnace. The RTA anneal allows the dopant, namely phosphorous, to diffuse into the substitutional lattice sites where they are electrically active.

The silicon nanoresonators are fabricated following the dopant activation. First, a layer of hydrogen silsesquioxane (HSQ) is spin-coated on top of the device layer. The silicon nanoresonators are then patterned with e-beam lithography

Manuscript received November 23, 2011; revised May 14, 2012 and July 15, 2012; accepted July 19, 2012. Date of publication August 7, 2012; date of current version November 16, 2012. This work was supported by the National Science Foundation under Grant 0826276. The review of this paper was arranged by Associate Editor Y. Arakawa.

L. Yu was with the Department of Physics, Purdue University and Birck Nanotechnology Center, West Lafayette, IN 47907 USA. He is now with the Applied Materials, Inc., Santa Clara, CA 95054 USA (e-mail: yulin@purdue.edu).

H. Pajouhi and S. Mohammadi are with the School of Electrical and Computer Engineering, Purdue University and Birck Nanotechnology Center, West Lafayette, IN 47907 USA (e-mail: hpajouhi@purdue.edu; saeedm@purdue.edu).

M. R. Nelis and J. F. Rhoads are with the School of Mechanical Engineering, Purdue University and Birck Nanotechnology Center, West Lafayette, IN 47907 USA (e-mail: mnelis@purdue.edu; jfrhoads@purdue.edu).

Color versions of one or more of the figures in this paper are available online at http://ieeexplore.ieee.org.

Digital Object Identifier 10.1109/TNANO.2012.2212028

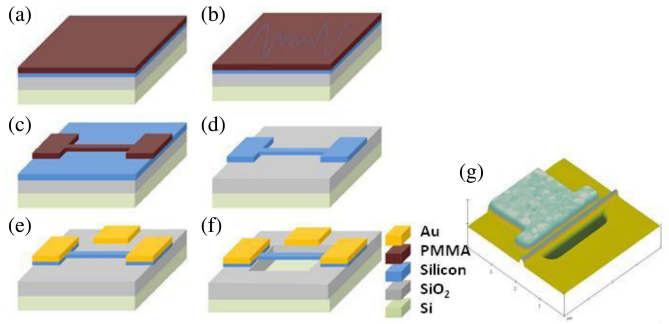

Fig. 1. Fabrication process flow of top-down silicon nanoresonators. (a) The process begins with an SOI wafer with a thin device layer. (b) The nanoresonators are patterned with e-beam lithography. (c) After development, HSQ is used as the etching mask for silicon dry etching. (d) The HSQ is removed with BOE etchant. (e) Cr/Au layers are deposited to form the metal contacts of the nanoresonators. (f) The trench is opened between source and drain and the nanoresonators are released by a CPD process after BOE oxide etching. (g) Atomic force micrograph of a suspended silicon nanoresonator fabricated using the SOI process flow.

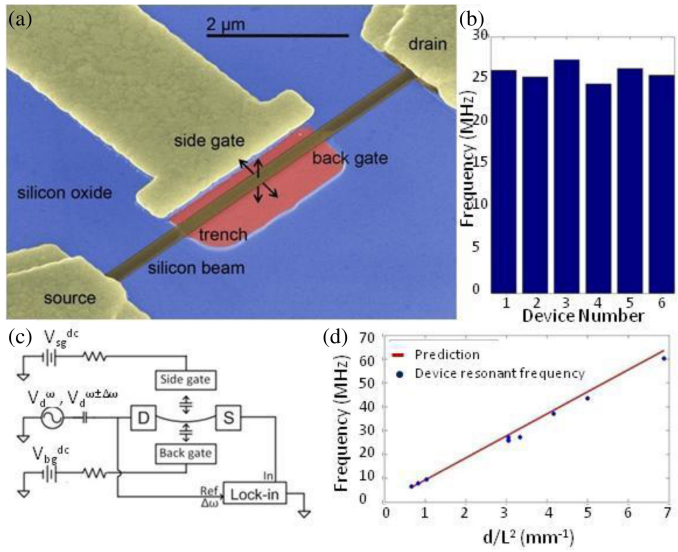

Fig. 2. (a) A scanning electron micrograph of a representative silicon nanoresonator fabricated using an SOI process flow. (b) Linear resonant frequencies of six nanoresonators with nominally identical geometries. (c) Diagram of the measurement setup. An amplitude-modulated (AM) high-frequency signal is applied on the drain electrode. The current from the NW is detected by a lock-in amplifier in the source port, at frequency $\Delta\omega$. The AM modulation frequency is 1 kHz. (d) Measured linear resonant frequencies of nine devices with different geometries and a comparison with theoretical prediction.

using HSQ as a high-resolution, negative-tone inorganic electron-beam resist. After development, the exposed HSQ remains on the wafer, which is then introduced into a reactive ion process. After plasma etching, the wafer is dipped in buffered oxide etchant (BOE) for 30 s to remove the HSQ. Another e-beam lithography process is then performed to define the source, drain, and side-gate electrodes. This is followed by metal deposition and a lift-off process. The thick metal contacts are realized with 30 nm chrome and 200 nm gold in order to achieve good step coverage of the silicon nanoresonators.

Note that a small window is patterned between source and drain with another e-beam lithography process and the SiO_2 beneath the resonators is etched in BOE. Finally, the suspended resonators are released through the use of a critical point drying (CPD) process. Fig. 1 shows the device fabrication process (a)–(f) and a typical atomic force microscopic image of a suspended silicon nanoresonator (g) fabricated with this process.

A scanning electron micrograph of a representative SOI-NEMS device is shown in Fig. 2. This nanoresonator features a near-rectangular cross section, measuring approximately 110 nm high and 120 nm wide, and is suspended approximately 144 nm above the bottom gate. Note that phosphorus implantation is used to enhance the conductance of the Si nanoresonators and reduce their contact resistance—key factors in reducing the thermoelectric noise floor of SOI-NEMS. Also of note is the unique dual-gate nature of this system, which allows in-plane and out-of-plane modes of vibration to be selectively actuated and detected through electrostatic mechanisms, ultimately enabling planar, nonplanar, and combination (e.g., whirling) motions [35]–[37].

III. Measurement Setup

To recover the near-resonant response of the dual-gate SOI devices, the measurement setup shown in Fig. 2(c) is employed. This system utilizes a high-vacuum chamber (ambient pressure $<10^{-4}$ torr) and an electrostatic measurement technique similar to that previously described in [4]. For this particular research, two distinct dc biases are applied on the side gate and back gate, and two ac signals, a pure sinusoid with frequency ω and another with carrier frequency ω and sinusoidal amplitude modulation at $\Delta\omega$, are applied to the drain electrode, facilitating motion and measurement readout. Due to the capacitance change induced by mechanical motion, the two ac signals mix together when their frequencies approach the natural frequency of the nanoresonator, enabling the vibration of the nanoresonator to be directly measured via the down-mixed current at the intermediate frequency $\Delta\omega$ using a lock-in amplifier at the source port. The lock-in amplifier is locked at frequency $\Delta\omega$ (1 kHz) and a Labview-based automated measurement setup is used to collect data and graph the results. As noted in subsequent sections, the detectable mixing current at frequency $\Delta\omega$, which is related to the physical displacement of the device, has two dominant components: a background response induced by the ac voltage applied to the drain and attributable to electrostatic field induced current modulation and a resonant response induced by mechanical motion and attributable to the conductance and piezoresistive changes caused by this motion [4], [38]. Mathematically, this results in a detectable mixing current given by

$$I^{\Delta\omega}(\omega) = \frac{dG}{dV_g}\left[V_{\rm ds}^2 + \frac{C_g' z(\omega)}{C_g} V_g V_{\rm ds}\right] \tag{1}$$

where $z(\omega)$ denotes the deflection of the center of the nanoresonator with respect to its equilibrium position, G is the nanoresonator's conductance, C_g' and C_g are the differential and absolute capacitances between the gate and device, respectively, and V_g and $V_{\rm ds}$ are the amplitudes of the gate bias and ac voltage applied to the drain, respectively. Note that the piezoresistive strain varies at twice of the resonant frequency of the device and

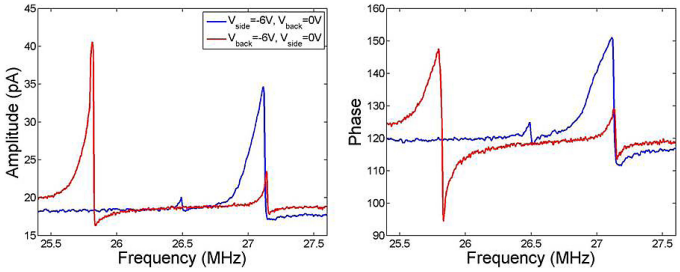

Fig. 3. Experimental frequency response obtained from a dual-gate nanoresonator, measuring approximately 120 nm wide, 110 nm thick, and 6.3 μm long, with a source–drain voltage of $V_{\rm ds} = 15$ mV$_{\rm rms}$ and $V_{\rm side} = -6$ V, $V_{\rm back} = 0$ V (blue) and $V_{\rm side} = 0$ V, $V_{\rm back} = -6$ V (red). Note that the lower frequency resonances correspond to out-of-plane vibrations, while the higher frequency resonances correspond to in-plane motions.

is thus not detected with the measurement technique utilized in this study [27]. Also note that the typical amplitude of the device's response is less than 10 nm, which corresponds to a capacitance change C_g' on the order of 10^{-19}–10^{-18} F.

IV. Experimental Results

Using the aforementioned measurement technique, a series of devices, with both identical and different dimensions, was characterized. Fig. 2(d) shows the extrapolated linear resonant frequencies (out-of-plane) of nine devices with different geometries, and a comparison with theoretical prediction. Likewise, Fig. 2(b) shows the measured linear resonant frequencies (out-of-plane) of six devices with nominally the same dimensions. The calculated average frequency for these nominally identical devices is 25.8 MHz, which is close to the predicted resonant frequency of 25.5 MHz. The standard deviation of the measurement is 0.96 MHz.

Fig. 3 depicts the frequency response (amplitude and phase of the measured mixing current versus excitation frequency) for a representative dual-gate silicon nanoresonator device actuated with a 15 mV$_{\rm rms}$ source-drain voltage $V_{\rm ds}$ under two different bias configurations. As evident, each response exhibits two distinct resonances. The lower frequency resonances, which occur in the proximity of the predicted natural frequency of 25.5 MHz, correspond to out-of-plane motions, while the higher frequency resonances, which occur in the proximity of the predicted natural frequency of 27.7 MHz, correspond to in-plane motions. Due to the dual-gate nature of the structure, these near-orthogonal motions can be selectively utilized, or used in conjunction with one another, in the course of near-resonant device operation [35]–[37]. Note that there is a measurable degree of coupling between these motions, largely due to the fringing electric fields generated by the two distinct gates. Also of note from Fig. 3 is the non-Lorentzian shape of the near-resonant response. This is indicative of the fact that the device is operating in a nonlinear frequency response regime, despite the comparatively small source–drain excitation voltage. Note that this observation is congruent with previous investigations of NEMS resonators operating in the presence of an elevated noise floor [39]. While the quality factor Q associated with resonance is ill-defined for nonlinear systems, a comparable metric, hereafter referred to as effective quality factor $Q_{\rm eff}$, can be estimated from this frequency response using the ratio of center frequency to full-width at half-maximum definition. Note that $Q_{\rm eff}$ is approximately 3000 for this device.

Fig. 3 also highlights the tunable nature of the dual-gate devices described herein, a topic discussed at length in the following section. Of particular note is the fact that the resonance frequencies, corresponding to in-plane and out-of-plane motions, shift under different bias conditions. These shifts are attributable to the fact that two distinct tuning mechanisms impact the response of doubly clamped, electrostatically transduced nanoresonators: a nonlinear stiffening (hardening) effect, which arises in the presence of large elastic deformations, and a linear and nonlinear capacitive (softening) effect, which is inherent to the variable-gap nature of the electrostatic actuation force [25], [34], [40]–[49]. When a dc bias voltage is applied on a gate and a potential difference is created, the resulting electrostatic force attracts the nanoresonator toward the gate, inducing tension in the resonator, a static deflection, and, generally, an increase in the nonlinear resonant frequency [defined as the frequency of maximum amplitude, or, analogously, the upper bifurcation (jump) frequency]. If the dc bias voltage is applied such that the resulting electrostatic force is predominantly in the same direction as the nanoresonator's motion, the bias also provides a capacitive softening effect, which typically reduces the resonant frequency. In the excitation scenarios depicted in Fig. 3, a hardening effect produced by the side gate shifts the out-of-plane resonances to higher frequencies, as seen by benchmarking the lower frequency resonance highlighted in red against that highlighted in blue. Likewise, a capacitive softening effect produced by the back gate shifts the in-plane resonances to lower frequencies, as seen by benchmarking the higher frequency resonances highlighted in blue against that highlighted in red.

V. Characterizing and Tuning the Nonlinear Response

The ability to finely control the linear and nonlinear frequency response characteristics of nanoresonators is essential to their implementation in practical applications, including sensing and signal processing, and for mitigating the effects of process-induced device variations in these settings.

The dual-gate nanoresonator structure detailed herein represents a highly tunable device platform as it facilitates planar, nonplanar, and combined (e.g., whirling) near-resonant motions, which can be tuned bidirectionally.

Fig. 4 depicts a representative near-resonant response of the nanoresonator at different side-gate biases when the back-gate bias is fixed, as acquired by incrementing the side-gate bias. The upper panels specifically highlight the magnitude of the detected mixing current, as a function of both the excitation frequency ω and the side-gate bias voltage $V_{\rm side}$ for three distinct back-gate biases $V_{\rm back}$. Note that a 15-mV$_{\rm rms}$ source–drain voltage was selected for actuation purposes here, as it is just strong enough to drive the near-resonant response above the noise floor (as set by thermomechanical effects and the employed measurement

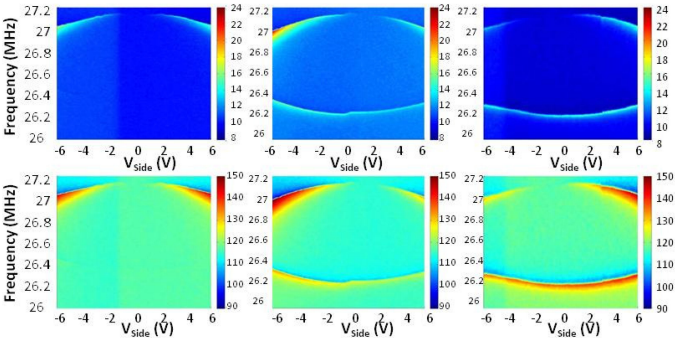

Fig. 4. Resonant response of a representative dual-gate nanoresonator at different side-gate bias voltages with a fixed bias on the back gate. The amplitude of the ac source–drain voltage excitation is 15 $\mathrm{mV_{rms}}$. The side-gate bias is changed from -6 V to 6 V in 0.1 V steps. The upper panels highlight the magnitude of the detected mixing current (in pA) as a function of both the excitation frequency ω and the side-gate bias voltage V_{side} for back-gate bias voltages V_{back} of 0, 3, and -3 V, respectively. The lower panels highlight the corresponding phase for $V_{\mathrm{back}} = 0$, 3, -3 V.

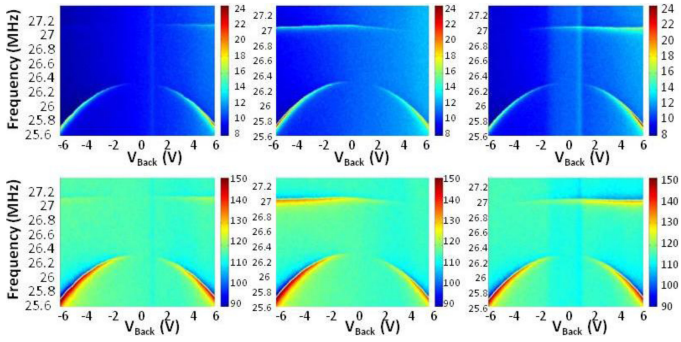

Fig. 5. Resonant response of a representative dual-gate nanoresonator at different back-gate bias voltages with a fixed bias on the side gate. The amplitude of the ac source–drain voltage excitation is 15 $\mathrm{mV_{rms}}$. The back-gate bias is changed from -6 V to 6 V in 0.1 V steps. The upper panels highlight the magnitude of the detected mixing current (in pA) as a function of both the excitation frequency ω and the back-gate bias voltage V_{back} for side-gate bias voltages V_{side} of 0, 3, and -3 V, respectively. The lower panels highlight the corresponding phase for $V_{\mathrm{side}} = 0$, 3, -3 V.

system). As evident, for each back-gate bias, two distinct resonant responses are observable: a comparatively high-frequency response corresponding to an in-plane mode of vibration, and a comparatively low-frequency response corresponding to out-of-plane motion. Also of note is that for each bias configuration, the background response is virtually independent of the dc biases applied on both the back and side gates. This allows the background amplitude to be extracted from experimental measurements, which, in turn, allows for direct comparisons of the near-resonant response.

When $V_{\mathrm{back}} = 0$ V, there is no detectable out-of-plane resonance above the noise floor. However, in-plane motions are easily observed. Of note is the fact that the resonance frequency decreases with increasing side-gate bias—a phenomenon consistent with the previously described capacitive softening mechanism. The lower left panel of Fig. 4 highlights the corresponding phase detected as a function of driving frequency and side-gate bias. Similar frequency tuning effects can be observed. Notably, both the frequency response and the amplitude of the mixing current are asymmetric with respect to the unbiased state, most likely due to residual stress within the nanoresonator or the asymmetric nature of the total electric field.

When $V_{\mathrm{back}} = 3$ V, both planar and nonplanar motions are detectable. As in the 0 V case, the resonance frequency associated with in-plane motion decreases with increasing side-gate bias. In contrast, the peak frequency associated with out-of-plane motions increases with increasing side-gate bias—a phenomenon consistent with the previously defined stiffening mechanism. The lower center panel of Fig. 4 depicts the corresponding phase change. As previously noted, the amplitude of the measured current is asymmetric with respect to the unbiased state. Similar phenomena are observed when $V_{\mathrm{back}} = -3$ V.

Fig. 5 highlights the resonant response obtained from a representative nanoresonator by fixing the side-gate bias and incrementing the back-gate bias. In general, the results recovered through this experimental analysis, mirror those described in Fig. 4, which were recovered by incrementing the side-gate bias.

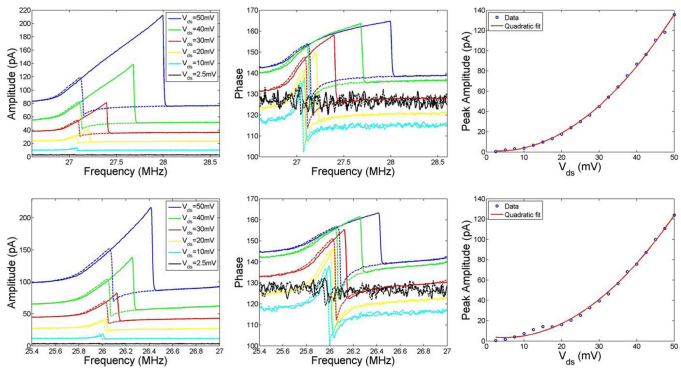

Fig. 6. (Top row) Near-resonant, planar response and (bottom row) nonplanar response of a representative silicon nanoresonator obtained by exciting the system with various ac source–drain voltages V_{ds}, while sweeping the excitation frequency ω up and down. The left column highlights the corresponding mixing current versus frequency trajectories at different source–drain excitation amplitudes by sweeping the excitation frequency up and down, respectively. The solid lines correspond to frequency sweeping up and the dashed lines correspond to frequency sweeping down. The center column highlights the corresponding phase change versus frequency trajectories at different source–drain excitation amplitudes. The right column shows the extracted peak amplitude as a function of the source–drain voltage amplitude (subtracting the background amplitude) as obtained by sweeping the frequency. One can see all of the response characteristics noted in planar response remain qualitatively unchanged with the nonplanar bias configuration.

However, one noticeable difference exists—capacitive softening mechanisms appear to dominate in all tuning scenarios.

Given the hysteretic nature of the nonlinear response of nanoresonators, a series of frequency sweeps were also initiated to characterize the devices' bifurcation structure and demonstrate how the structures can be tuned by varying the voltage biases applied to the back and side gates. This capability is essential for the development of small-scale resonators which actively exploit nonlinear effects in applications such as resonant mass sensing and signal processing, as previously demonstrated at the microscale [40], [50]–[52].

Fig. 6 (top row) highlights the near-resonant response associated with the planar vibrations of a representative dual-gate

resonator as recovered by incrementing the applied source–drain voltage $V_{\rm ds}$ and sweeping the excitation frequency up and down. Note that the gate biases are fixed such that $V_{\rm back} = 0$ V and $V_{\rm side} = 5$ V to ensure that the back-gate bias does not affect the in-plane motion. As evident, the system exhibits a Duffing-like [53] response characteristic, bistability over a finite frequency bandwidth, and hysteresis with respect to the direction of the frequency sweep. The left and center panels highlight the detected mixing current and corresponding phase change as $V_{\rm ds}$ is increased. Note that $V_{\rm ds} = 2.5$ mV approximates the thermomechanical/thermoelectric noise floor of the measured system. Under such a low source–drain voltage, the peak resonance response [proportional to $V_{\rm ds}$ as seen from (1)] and the background electrostatic field current modulation (proportional to $V_{\rm ds}^2$) become comparable to the noise floor of the system. Contributing noise sources to the noise floor in the system, as discussed in [54], include Johnson noise from the resonator and the lock-in amplifier, 1/f noise, thermomechanical noise, adsorption–desorption noise, and defect motion noise. This figure reveals that with increasing $V_{\rm ds}$ the bandwidth and center frequency of the hysteretic region increase in a consistent manner—a mechanism that can be advantageously leveraged in practical application. The right panel depicts the extracted peak amplitude as a function of the source–drain voltage amplitude (subtracting the background amplitude) as obtained by sweeping the frequency.

Similar nonlinear behavior to that detailed in Fig. 6 (top row) is observed for the nonplanar vibrations as well. In this experimental analysis, the gate biases are fixed such that $V_{\rm back} = 5$ V and $V_{\rm side} = 0$ V, and the amplitude of the ac source–drain voltage is incremented. Fig. 6 (bottom row) shows the nonplanar response when $V_{\rm ds}$ is increased. Generally speaking, all of the response characteristics noted in Fig. 6 (top row) remain qualitatively unchanged with this bias configuration.

To further characterize the nonlinear frequency response structure, the device's back-gate bias is fixed at zero and the side-gate bias was incremented from -5 V to 5 V, with the upper and lower bifurcation (jump) frequencies being recorded at each step. Fig. 7 shows the results of this experimental analysis when (left) negative and (right) positive dc biases are applied. As evident, for small ac source–drain voltages, no hysteresis is observed. However, at modest source–drain voltages, hysteresis (nonlinearity) occurs. As the side-gate bias is increased, the apex of each bifurcation wedge shifts to lower frequencies, due to a capacitive softening effect. Simultaneously, the top of each wedge shifts toward higher frequencies, indicating an increased frequency bandwidth associated with hysteresis at higher ac source–drain voltages. Note that the onset of nonlinearity can be easily characterized by a critical voltage excitation amplitude, which is defined to be the point at which the frequency response structure features an infinite slope [39]. Using this criteria in the context of Fig. 7 allows the critical amplitude to be defined as the source–drain voltage at which the frequency trajectories recovered via upsweep and downsweep start to deviate from each other for a given gate bias. Examining the right panel, as an example, allows one to conclude that the critical excitation amplitude is approximately $V_{\rm ds} = 5$ mV for $V_{\rm side} = 5$ V for the devices considered here.

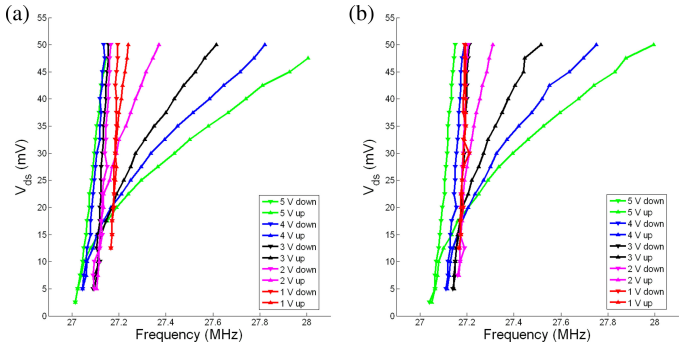

Fig. 7. Bifurcation diagrams, constructed by experimentally locating upper and lower jump bifurcations, highlighting the nonlinear characteristics associated with planar vibration. The panels highlight the system's tunability with (left) negative side-gate biases and (right) positive side-gate biases, respectively. Note that as the side-gate bias $V_{\rm side}$ is increased, the apex of each bifurcation wedge shifts to lower frequencies, due to a capacitive softening effect. Simultaneously, the top of each wedge shifts toward higher frequencies, indicating an increased frequency bandwidth associated with hysteresis at higher ac source–drain voltages $V_{\rm ds}$.

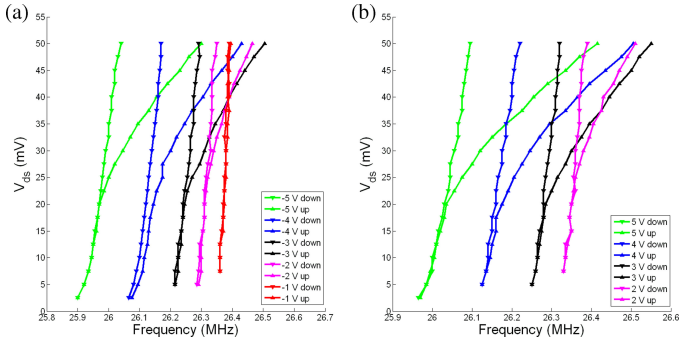

Fig. 8. Bifurcation diagrams, constructed by experimentally locating upper and lower jump bifurcations, highlighting the nonlinear characteristics associated with out-of-plane vibration. The insets highlight the system's tunability with (a) negative back-gate biases and (b) positive back-gate biases, respectively. Note that as the back-gate bias $V_{\rm back}$ is increased, the apex of each bifurcation wedge shifts toward lower frequencies, due to a capacitive softening effect. Simultaneously, the top of each wedge shifts towards higher frequencies, indicating an increased frequency bandwidth associated with hysteresis at higher ac source–drain voltages $V_{\rm ds}$.

Similarly, Fig. 8 highlights the bifurcation structure associated with out-of-plane device motions when the side-gate bias is fixed at zero and the back-gate bias is incremented from -5 V to 5 V. Again, the qualitative characteristics observed for planar motions appear to remain in the case of nonplanar motion.

VI. Conclusion

To the best of the authors' knowledge, this study represents the first demonstration of dual-gate, nonlinear nanoelectromechanical resonators based upon an SOI process flow. As the proposed devices can be seamlessly, reproducibly, and reliably fabricated and integrated with commercial CMOS technologies, this advancement will enable the design and development of future nanosystems, specifically those targeting sensing and signal processing applications.

A key characteristic of the nanoresonators detailed herein is their inherently nonlinear and tunable nature. The systems typically exhibit a Duffing-like frequency response characteristic when excited above the noise floor, and thus exhibit hysteresis with respect to the excitation frequency over a finite bandwidth. This behavior should not be seen as detriment however, as it is highly tunable. Accordingly, it should enable the development of highly sensitive bifurcation-based mass sensors, narrow-band amplifiers, and highly selective tunable receivers [52].

ACKNOWLEDGMENT

The authors would like to thank Profs. A. Raman and Y. Chen for their collaboration and useful discussions.

REFERENCES

[1] K. L. Ekinci and M. L. Roukes, "Nanoelectromechanical systems," *Rev. Sci. Instrum.*, vol. 76, no. 6, pp. 061101-1–061101-12, 2005.

[2] X. L. Feng, R. He, P. Yang, and M. L. Roukes, "Very high frequency silicon nanowire electromechanical resonators," *Nano Lett.*, vol. 7, no. 7, pp. 1953–1959, 2007.

[3] H. Peng, C. Chang, S. Aloni, T. Yuzvinsky, and A. Zettl, "Ultrahigh frequency nanotube resonators," *Phys. Rev. Lett.*, vol. 97, no. 8, pp. 2–5, 2006.

[4] V. Sazonova, Y. Yaish, H. Ustünel, D. Roundy, T. A. Arias, and P. L. McEuen, "A tunable carbon nanotube electromechanical oscillator," *Nature*, vol. 431, no. 7006, pp. 284–287, 2004.

[5] X. M. H. Huang, X. L. Feng, C. A. Zorman, M. Mehregany, and M. L. Roukes, "VHF, UHF and microwave frequency nanomechanical resonators," *New J. Phys.*, vol. 7, no. 1, pp. 247–247, 2005.

[6] A. Erbe, H. Crommer, A. Kraus, and R. H. Blick, "Mechanical mixing in nonlinear nanomechanical resonators," *Appl. Phys. Lett.*, vol. 77, no. 19, pp. 3102–3104, 2000.

[7] L. Rabieirad and S. Mohammadi, "Single-walled carbon nanotube mixers," in *Proc. IEEE MTT-S Int. Microwave Symp. Dig.*, Jun. 2006, pp. 2055–2058.

[8] R. Almog, S. Zaitsev, O. Shtempluck, and E. Buks, "Signal amplification in a nanomechanical Duffing resonator via stochastic resonance," *Appl. Phys. Lett.*, vol. 90, no. 1, pp. 013508-1–013508-3, 2007.

[9] R. Almog, S. Zaitsev, O. Shtempluck, and E. Buks, "Noise squeezing in a nanomechanical Duffing resonator," *Phys. Rev. Lett.*, vol. 98, no. 7, pp. 1–4, 2007.

[10] A. N. Cleland and M. L. Roukes, "A nanometre-scale mechanical electrometer," *Nature*, vol. 392, no. 6672, pp. 160–162, 1998.

[11] K. L. Ekinci, X. M. H. Huang, and M. L. Roukes, "Ultrasensitive nanoelectromechanical mass detection," *Appl. Phys. Lett.*, vol. 84, no. 22, pp. 4469–4471, 2004.

[12] B. Ilic, "Attogram detection using nanoelectromechanical oscillators," *J. Appl. Phys.*, vol. 95, no. 7, pp. 3694–3703, 2004.

[13] B. Ilic, Y. Yang, and H. G. Craighead, "Virus detection using nanoelectromechanical devices," *Appl. Phys. Lett.*, vol. 85, no. 13, pp. 2604–2606, 2004.

[14] K. Jensen, K. Kim, and A. Zettl, "An atomic-resolution nanomechanical mass sensor," *Nature Nanotechnol.*, vol. 3, no. 9, pp. 533–537, 2008.

[15] G. Abadal, Z. J. Davis, B. Helbo, and X. Borris, "Electromechanical model of a resonating nano-cantilever-based sensor for high-resolution and high-sensitivity mass," *Nanotechnology*, vol. 100, no. 12, pp. 100–104, 2001.

[16] E. Buks and B. Yurke, "Mass detection with a nonlinear nanomechanical resonator," *Phys. Rev. E*, vol. 74, no. 4, pp. 1–9, 2006.

[17] N. V. Lavrik, M. J. Sepaniak, and P. G. Datskos, "Cantilever transducers as a platform for chemical and biological sensors," *Rev. Sci. Instrum.*, vol. 75, no. 7, pp. 2229–2253, 2004.

[18] Z. J. Davis, G. Abadal, O. Kuhn, O. Hansen, F. Grey, and A. Boisen, "Fabrication and characterization of nanoresonating devices for mass detection," *J. Vac. Sci. Technol. B*, vol. 18, no. 2, pp. 612–616, 2000.

[19] X. M. H. Huang, M. Manolidis, S. C. Jun, and J. Hone, "Nanomechanical hydrogen sensing," *Appl. Phys. Lett.*, vol. 86, no. 14, pp. 143104-1–143104-3, 2005.

[20] Y. T. Yang, C. Callegari, X. L. Feng, K. L. Ekinci, and M. L. Roukes, "Zeptogram-scale nanomechanical mass sensing," *Nano Lett.*, vol. 6, no. 4, pp. 583–586, 2006.

[21] K. Aihara, J. Xiang, S. Chopra, A. Pham, and R. Apprao, "GHz carbon nanotube resonator bio-sensors," in *Proc. IEEE 3rd Conf. Nanotechnol.*, Aug. 2003, vol. 2, pp. 612–614.

[22] B. Lassagne, D. Garcia-Sanchez, A. Aguasca, and A. Bachtold, "Ultrasensitive mass sensing with a nanotube electromechanical resonator," *Nano Lett.*, vol. 8, no. 11, pp. 3735–3738, 2008.

[23] A Husain, J. Hone, H. W. C. Postma, X. M. H. Huang, T. Dranke, M. Barbic, A. Scherer, and M. L. Roukes, "Nanowire-based very-high-frequency electromechanical resonator," *Appl. Phys. Lett.*, vol. 83, no. 6, pp. 1240–1242, 2003.

[24] D. Garcia-Sanchez, A. San Paulo, M. J. Esplandiu, F. Perez-Murano, L. Forro, A. Aguasca, and A. Bachtold, "Mechanical detection of carbon nanotube resonator vibrations," *Phys. Rev. Lett.*, vol. 99, no. 8, pp. 1–4, 2007.

[25] W. Y. Fung, E. N. Dattoli, and W. Lu, "Radio frequency nanowire resonators and *in situ* frequency tuning," *Appl. Phys. Lett.*, vol. 94, no. 20, pp. 203104-1–203104-3, 2009.

[26] G. A Steele, A. K. Huttel, B. Witkamp, M. Poot, H. B. Meerwaldt, L. P. Kouwenhoven, and H. S. J. van der Zant, "Strong coupling between single-electron tunneling and nanomechanical motion," *Science*, vol. 325, no. 5944, pp. 1103–1107, 2009.

[27] R. He, X. L. Feng, M. L. Roukes, and P. Yang, "Self-transducing silicon nanowire electromechanical systems at room temperature," *Nano Lett.*, vol. 8, no. 6, pp. 1756–1761, 2008.

[28] J. M. Nichol, E. R. Hemesath, L. J. Lauhon, and R. Budakian, "Controlling the nonlinearity of silicon nanowire resonators using active feedback," *Appl. Phys. Lett.*, vol. 95, no. 12, pp. 123116-1–123116-3, 2009.

[29] A. K. Naik, M. S. Hanay, W. K. Hiebert, X. L. Feng, and M. L. Roukes, "Towards single-molecule nanomechanical mass spectrometry," *Nature Nanotechnol.*, vol. 4, no. 7, pp. 445–450, 2009.

[30] A. N. Cleland and M. L. Roukes, "Fabrication of high frequency nanometer scale mechanical resonators from bulk Si crystals," *Appl. Phys. Lett.*, vol. 69, no. 18, pp. 2653–2655, 1996.

[31] P. A. Truitt, J. B. Hertzberg, C. C. Huang, K. L. Ekinci, and K. C. Schwab, "Efficient and sensitive capacitive readout of nanomechanical resonator arrays," *Nano Lett.*, vol. 7, no. 1, pp. 120–126, 2007.

[32] A. N. Cleland and M. L. Roukes, "External control of dissipation in a nanometer-scale radiofrequency mechanical resonator," *Sens. Actuators, A*, vol. 72, no. 3, pp. 256–261, 1999.

[33] D. N. Guerra, T. Dunn, and P. Mohanty, "Signal amplification by 1/f noise in silicon-based nanomechanical resonators," *Nano Lett.*, vol. 9, no. 9, pp. 3096–3099, 2009.

[34] C. Durand, F. Casset, P. Renaux, N. Abele, B. Legrand, D. Renaud, E. Ollier, P. Ancey, A. M. Ionescu, and L. Buchaillot, "In-plane silicon-on-nothing nanometer-scale resonant suspended gate MOSFET for In-IC integration perspectives," *IEEE Electron Device Lett.*, vol. 29, no. 5, pp. 494–496, May 2008.

[35] W. G. Conley, A. Raman, C. M. Krousgrill, and S. Mohammadi, "Nonlinear and nonplanar dynamics of suspended nanotube and nanowire resonators," *Nano Lett.*, vol. 8, no. 6, pp. 1590–1595, 2008.

[36] W. G. Conley, L. Yu, M. R. Nelis, A. Raman, C. M. Krousgrill, S. Mohammadi, and J. F. Rhoads, "The nonlinear dynamics of electrostatically-actuated, single-walled carbon nanotube resonators," in *Proc. 10th Int. Conf. Recent Adv. Struct. Dyn.*, 2010, pp. 65-1–65-12.

[37] H. M. Ouakad and M. I. Younis, "Nonlinear dynamics of electrically actuated carbon nanotube resonators," *ASME J. Comput. Nonlinear Dyn.*, vol. 5, no. 1, pp. 011009-1–011009-13, 2010.

[38] V. A. Sazonova, "Tunable carbon nanotube resonator," Ph.D. dissertation, Dept. Phys., Cornell Univ., Ithaca, NY, 2006.

[39] H. W. C. Postma, I. Kozinsky, A. Husain, and M. L. Roukes, "Dynamic range of nanotube- and nanowire-based electromechanical systems," *Appl. Phys. Lett.*, vol. 86, no. 22, pp. 223105-1–223105-3, 2005.

[40] B. E. DeMartini, J. F. Rhoads, K. L. Turner, S. W. Shaw, and J. Moehlis, "Linear and nonlinear tuning of parametrically excited MEMS oscillators," *J. Microelectromech. Syst.*, vol. 16, no. 2, pp. 310–318, 2007.

[41] I. Kozinsky, H. W. C. Postma, I. Bargatin, and M. L. Roukes, "Tuning nonlinearity, dynamic range, and frequency of nanomechanical resonators," *Appl. Phys. Lett.*, vol. 88, no. 25, pp. 253101-1–253101-3, 2006.

[42] S. Purcell, P. Vincent, C. Journet, and V. Binh, "Tuning of nanotube mechanical resonances by electric field pulling," *Phys. Rev. Lett.*, vol. 89, no. 27, pp. 1–4, 2002.

[43] K. Schwab, "Spring constant and damping constant tuning of nanomechanical resonators using a single-electron transistor," *Appl. Phys. Lett.*, vol. 80, no. 7, pp. 1276–1278, 2002.
[44] W. G. Conley, "Nonlinear dynamics in nanomechanical systems," PhD dissertation, Purdue Univ., Sch. Mech. Eng., West Lafayette, IN, 2009.
[45] C. C. Wu and Z. Zhong, "Capacitive spring softening in single-walled carbon nanotube nanoelectromechanical resonators," *Nano Lett.*, vol. 11, no. 4, pp. 1448–1451, 2011.
[46] D. W. Carr, "Measurement of nanomechanical resonant structures in single-crystal silicon," *J. Vac. Sci. Technol. B*, vol. 16, no. 6, pp. 3821–3824, 1998.
[47] L. Sekaric, J. M. Parpia, H. G. Craighead, T. Feygelson, B. H. Houston, and J. E. Butler, "Nanomechanical resonant structures in nanocrystalline diamond," *Appl. Phys. Lett.*, vol. 81, no. 23, pp. 4455–4457, 2002.
[48] X. L. Feng, M. H. Matheny, R. B. Karabalin, C. A. Zorman, M. Mehregany, and M. L. Roukes, "Silicon carbide (SiC) top-down nanowire electromechanical resonators," in *Proc. Solid-State Sensors, Actuators, Microsystems Conf.*, Jun. 2009, pp. 2246–2249.
[49] T. Kouh, O. Basarir, and K. L. Ekinci, "Room-temperature operation of a nanoelectromechanical resonator embedded in a phase-locked loop," *Appl. Phys. Lett.*, vol. 87, no. 11, pp. 113112-1–113112-3, 2005.
[50] J. F. Rhoads, S. W. Shaw, K. L. Turner, and R. Baskaran, "Tunable microelectromechanical filters that exploit parametric resonance," *J. Vib. Acoust.*, vol. 127, no. 5, pp. 423–430, 2005.
[51] J. F. Rhoads, S. Shaw, K. Turner, J. Moehlis, B. Demartini, and W. Zhang, "Generalized parametric resonance in electrostatically actuated microelectromechanical oscillators," *J. Sound Vib.*, vol. 296, no. 4–5, pp. 797–829, 2006.
[52] V. Kumar, J. W. Boley, Y. Yang, H. Ekowaluyo, J. K. Miller, G. T.-C. Chiu, and J. F. Rhoads, "Bifurcation-based mass sensing using piezoelectrically-actuated microcantilevers," *Appl. Phys. Lett.*, vol. 98, no. 15, pp. 153510-1–153510-3, 2011.
[53] J. F. Rhoads, S. W. Shaw, and K. L. Turner, "Nonlinear dynamics and its applications in micro- and nanoresonators," *J. Dyn. Syst. Meas. Control*, vol. 132, no. 3, pp. 034001-1–034001-14, 2010.
[54] A. N. Cleland and M. L. Roukes, "Noise processes in nanomechanical resonators," *J. Appl. Phys.*, vol. 92, no. 5, pp. 2758–2769, 2002.

Lin Yu received the B.S. degree in physics from the University of Science and Technology of China, Hefei, China in 2001, and the M.S. and Ph.D. degrees in physics from Purdue University, West Lafayette, IN, in 2008 and 2011, respectively.

He is currently a Process Engineer at Applied Materials, Inc., Santa Clara, CA. His specialty is semiconducting plasma etching, surface processing, and reaction engineering.

Hossein Pajouhi received the B.S. degree in electrical engineering from the University of Tehran, Tehran, Iran. He is currently working toward the Ph.D. degree in electrical engineering at Purdue University, West Lafayette, IN.

His research interests focus on nanoelectromechanical systems.

Molly R. Nelis (M'08) received B.S. degrees in electrical engineering and mechanical engineering from the Rose-Hulman Institute of Technology, Terre Haute, IN in 2009, and the M.S. degree in mechanical engineering from Purdue University, West Lafayette, IN in 2011 under the supervision of J. Rhoads. She is currently working toward the Ph.D. degree in mechanical engineering at the same institution under the supervision of D. Peroulis.

She was an Intern at Doctor's Orders Medical Engineering, Texas Instruments, and Los Alamos National Laboratories. Her research interests include the development of microelectromechanical system sensors, and the interface of mechanical and electrical engineering.

Mrs. Nelis is a member of the American Society of Mechanical Engineers, Society of Women Engineers, and Eta Kappa Nu.

Jeffrey F. Rhoads received the B.S., M.S., and Ph.D. degrees from Michigan State University, East Lansing, MI, in 2002, 2004, and 2007, respectively, all in mechanical engineering.

He is currently an Associate Professor in the School of Mechanical Engineering, Purdue University, West Lafayette, IN, affiliated with both the Birck Nanotechnology Center and Ray W. Herrick Laboratories. His current research interests include the predictive design, analysis, and implementation of resonant micro/nanoelectromechanical systems for use in chemical and biological sensing, electromechanical signal processing, and computing, the dynamics of parametrically excited systems and coupled oscillators, and the behavior of electromechanical systems operating in rich, multiphysics environments.

Dr. Rhoads is a member of the American Society for Engineering Education and the American Society of Mechanical Engineers, where he serves on the Student Design Committee and the Design Engineering Division's Technical Committees on Micro/Nanosystems and Vibration and Sound. He was the recipient of the National Science Foundation's Faculty Early Career Development (CAREER) Award and the Purdue University School Mechanical Engineering's Harry L. Solberg Best Teacher Award in 2009. He was also the recipient of the ASEE Mechanics Division's Ferdinand P. Beer and E. Russell Johnston, Jr. Outstanding New Mechanics Educator Award in 2011.

Saeed Mohammadi (SM'02) received the Ph.D. degree in electrical engineering from the University of Michigan, Ann Arbor, MI, in 2000.

He is currently an Associate Professor of electrical and computer engineering at Purdue University, West Lafayette, IN. His group is involved in research on RF devices and circuits and nanoelectronic technology.